Thermal transport, magnetism, and quantum oscillations in Weyl semimetal BaMnSb$_2$

Silu Huang, Lingyi Xing, Ramakanta Chapai, Roshan Nepal ⬤, and Rongying Jin ⬤
Department of Physics and Astronomy, Louisiana State University, Baton Rouge, Louisiana 70803, USA

Topological semimetals host unique electronic phases with either Dirac or Weyl characteristic. One way to obtain the Weyl phase is to break the time-reversal symmetry by establishing magnetic ordering. We have investigated the electrical and magnetic properties of a magnetic Weyl semimetal candidate BaMnSb$_2$ under the application of magnetic field (H) up to 35 T. We find that BaMnSb$_2$ undergoes three magnetic phase transitions with a ferromagnetic transition at $T_C \sim 690$ K and two antiferromagnetic transitions at $T_{N1} \sim 286$ K and $T_{N2} \sim 450$ K. At low temperatures, both the Shubnikov-de Haas and de Haas-van Alphen oscillations are observed by applying H along the c axis of BaMnSb$_2$. Data analysis indicates that the oscillations result from a single band, and the system can reach the first Landau level at high H. Evidence for Zeeman splitting is also observed at low Landau levels, which yields the Landé factor $g \sim 8.9 - 10.4$. In addition, thermal property measurements reveal very low phonon thermal conductivity and moderate thermopower. The coupling between charge, spin and lattice is discussed.

I. INTRODUCTION

Topological semimetals, including Dirac and Weyl types, have attracted great attention due to their exotic quantum properties. With linear energy dispersion in the momentum space, Dirac and Weyl semimetals host relativistic quasiparticles, which are described by Dirac and Weyl equations, respectively [1,2]. When the time-reversal symmetry or inversion symmetry is broken, Dirac semimetals evolve into Weyl semimetals [3]. As any magnetic ordering would break the time-reversal symmetry, magnetic compounds with Dirac-type band crossing are promising candidates for hosting Weyl fermions. Under such guidance, there has been enormous interest in the so-called 112-type Mn-based compounds with the general formula AMnPn$_2$, where A = Ca, Sr, Ba, Eu, Yb, and Pn = Sb, Bi [4–12]. In addition to magnetic ordering typically around room temperature, the Shubnikov-de Hass (SdH) and de Haas-van Alphen (dHvA) oscillations derive the nearly zero effective mass, high mobility, and nontrivial Berry phase, which are the characteristics of Dirac and Weyl fermions [4,5,7,9,13].

However, magnetism is necessary but often insufficient to realize the Weyl state. There is an accumulated experimental evidence for the inquiry of specific spin structure [9,13,14]. For example, quantum oscillations are absent in the collinearly ordered antiferromagnetic (AFM) state but emerge in the Eu canted AFM state in EuMnBi$_2$ [15]. Similarly, BaMnSb$_2$ possesses the canted AFM structure below $\sim$286 K with a ferromagnetic (FM) component in the ab plane [14]. The SdH oscillations are observed in the in-plane (ρ_{ab}), out-of-plane (ρ_c), and Hall (ρ_{xy}) resistivities [14,16]. By applying magnetic field along the c axis, data analysis reveals nearly zero effective mass (m^*), high mobility (μ_H) and nontrivial Berry phase (ϕ_B) [14,16]. Under 14 T, electrons can be pushed down to the second Landau level ($n = 2$) [14,16]. In this work, we present the magnetization, magnetic torque, magnetoresis-

tance, and Hall resistivity measurements of BaMnSb$_2$ under much wider temperature and magnetic field range. Several new features are observed. First, in addition to the known AFM transition at $T_{N1} \sim 286$ K, there are two other magnetic transitions with another AFM transition at $T_{N2} \sim 450$ K and a FM transition at $T_C \sim 690$ K. Second, the magnetic torque oscillation occurs only when $H \parallel c$, and its angle dependence indicates that the spin canting angle below T_{N1} is $\sim$50° with respect to the c axis. Third, high magnetic field allows the system to reach the first Landau level, at which there is evidence for the Zeeman splitting. In addition, the system exhibits low phonon thermal conductivity but moderate thermopower, important for understanding the underlying physics of BaMnSb$_2$.

II. EXPERIMENTAL DETIALS

Stoichiometric BaMnSb$_2$ Single crystals were grown through the floating zone technique with details described in Ref. [14]. The structure of our samples was analyzed by employing both powder and single crystal x-ray diffraction, revealing the tetragonal structure with the I4/mmm symmetry. The lattice parameters are $a = b = 4.556$ Å and $c = 24.299$ Å at room temperature. Below 400 K, the field and temperature dependence of the magnetization measurements were carried out in a *Quantum Design* 7-T Magnetic Property Measurement System (MPMS). High-temperature (300 K $\leqslant$ $T \leqslant 1000$ K) magnetization measurements were performed by a vibrating sample magnetometer (VSM) in Physical Property Measurement System (PPMS) by *Quantum Design*. Both the thermal conductivity and thermopower were measured in PPMS as well. The magnetic torque (τ) was measured using a piezoresistive torque magnetometer at National High Magnetic Field Lab (NHMFL) Tallahassee. A crystal was installed on a rotating platform allowing to continuously vary the angle between the magnetic field and the c axis of the crystal.
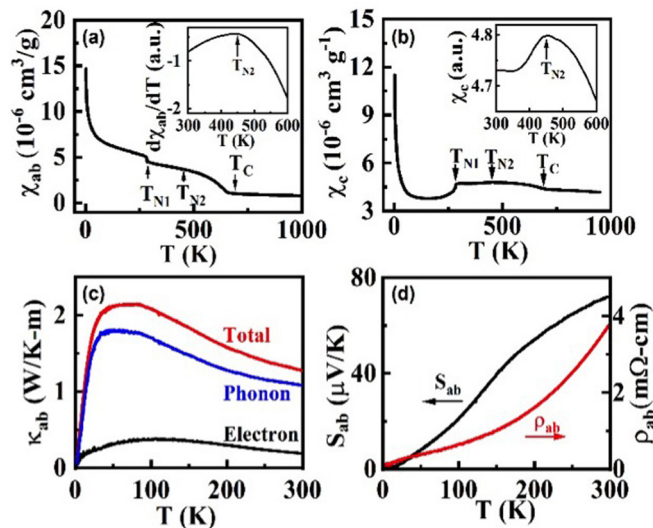
FIG. 1. (a) Temperature dependence of the magnetic susceptibility $\chi_{ab}(H \parallel ab)$. (Inset) Temperature derivative of $\chi_{ab}(T)$ as a function of temperature between 300 and 600 K with the indication of T_{N2}. (b) Temperature dependence of the magnetic susceptibility $\chi_c (H \parallel c)$. (Inset) $\chi_c(T)$ between 300 and 600 K with the indication of T_{N2}. (c) Temperature dependence of the in-plane thermal conductivity κ_{ab} (red), the electron contribution (black), and the phonon contribution (blue). (d) Temperature dependence of the thermopower (black) and in-plane resistivity ρ_{ab} (red).

The magnetotransport measurements, including $\rho_{ab}(H)$ and $\rho_{xy}(H)$, were also carried out at NHMFL using the standard four-probe technique by sweeping the field between -35 to $+35$ T.

III. RESULTS AND DISCUSSION

Figures 1(a) and 1(b) show the temperature dependence of the magnetic susceptibility of BaMnSb$_2$ for $H \parallel ab$ (χ_{ab}) and $H \parallel c$ (χ_c), respectively. In addition to the canted AMF transition at $T_{N1} \sim 286$ K, as reported previously [14], there are two other magnetic transitions. One occurs at $T_{N2} \sim 450$ K, below which $\chi_c(T)$ decreases with decreasing temperature [see the inset of Fig. 1(b)]. Although the change in $\chi_{ab}(T)$ is less obvious, the response can be seen in $d\chi_{ab}/dT$, which starts to increase in magnitude with decreasing temperature below T_{N2} [see the inset of Fig. 1(a)]. Another transition occurs at $T_C \sim 690$ K, below which both $\chi_{ab}(T)$ and $\chi_c(T)$ increase with decreasing temperature. We thus consider the ferromagnetic transition at T_C.

While it is magnetically ordered, the electrical resistivity shows no obvious anomaly at T_{N1} at zero filed [14], suggesting little spin-charge scattering in BaMnSb$_2$. This is also reflected in thermal transport properties. Figs. 1(c) and 1(d) show the temperature dependence of the in-plane thermal conductivity (κ_{ab}), thermopower (S_{ab}), respectively. Note that there is no obvious anomaly in either $\kappa_{ab}(T)$ and $S_{ab}(T)$ at T_{N1}. Overall, $\kappa_{ab}(T)$ exhibits a typical temperature dependence for a crystalline material, that initially increases then decreases with decreasing temperature. Quantitatively, κ_{ab} is small compared to other solids. Since there is no obvious contribution from spins, we consider that $\kappa_{ab} \sim \kappa_{\mathrm{electron}} + \kappa_{\mathrm{phonon}}$. Using the Wiedemann-Franz law, we can estimate the electronic thermal conductivity $\kappa_{\mathrm{electron}} = L_0T/\rho_{ab}$, where $L_0 = 2.44 \times 10^{-8}$ W Ω K^{-2} and ρ_{ab} is the in-plane electrical resistivity [see Fig. 1(d)]. As shown in Fig. 1(c), $\kappa_{\mathrm{electron}}$ is much smaller than the total κ_{ab}, suggesting phonon dominant thermal transport, i.e., $\kappa_{\mathrm{phonon}} = \kappa_{ab} - \kappa_{\mathrm{electron}}$. As shown in Fig. 1(c), $\kappa_{\mathrm{phonon}} \sim 1.0$ W K^{-1} m^{-1} at $T = 300$ K. Such small phonon thermal conductivity was also obtained in Ca$_{10}$Pt$_4$As$_8$(Fe$_2$As$_2$)$_2$, which forms a natural superlattice structure and contains plane and point defects [17]. Although the structure of BaMnSb$_2$ is less complex than Ca$_{10}$Pt$_4$As$_8$(Fe$_2$As$_2$)$_2$, its layered structure and possible defects as seen in its sister compound SrMnSb$_2$ [10] could be the origin for the small phonon thermal conductivity. Such property is extremely desirable for possible thermoelectric applications. However, the thermopower is moderate at room temperature as shown in Fig. 1(d). The positive S_{ab} is consistent with the Hall effect data [14], confirming hole-type conduction. Given the temperature dependence of both $\kappa_{ab}(T)$ and $S_{ab}(T)$ up to room temperature, it is possible that $S_{ab}(T)$ will continuously increase and $\kappa_{ab}(T)$ will further decease with increasing temperature, so to obtain high figure of merit at high temperatures.

When one investigates the high-temperature physical properties of BaMnSb$_2$, special attention should be paid to possible chemical changes. According to the recent experimental work on SrMnSb$_2$, there is evidence for the formation of SrO and MnSb at the surface [10]. The ferromagnetic (FM) transition at 580 K observed in SrMnSb$_2$ is thus attributed to MnSb [10]. If similar chemical transformation occurred in BaMnSb$_2$, one would expect the same T_C value as seen in SrMnSb$_2$ [10] and MnSb [18]. As shown in Figs. 1(a) and 1(b), the T_C value we obtained for BaMnSb$_2$ is much higher than the Curie temperature (~ 585 K) of MnSb [18]. This suggests that the FM behavior in BaMnSb$_2$ has different origin. According to earlier study, the FM saturation moment decreases with increasing Mn deficiency in Sr$_{1-y}$Mn$_{1-z}$Sb$_2$ [13]. At present, it is unclear whether the chemical nonstoichiometry causes different magnetic behavior besides possible MnSb formation at high temperatures. Despite different magnetic behavior at high temperatures, many 112-type compounds AMnPn$_2$ ($A =$ Ca, Sr, Ba, Eu, Yb, and Pn = Sb, Bi) exhibit canted AFM ordering at low temperatures [5,7,9,11,13,15,19], which is essential for nontrivial topological properties [14,15].

To further understand the nature of the magnetic properties of BaMnSb$_2$ at low temperatures, we have measured the field dependence of the magnetic torque $\tau(H)$ at 2 K, with the magnetic field applied in various directions. Figures 2(a) and 2(b) display the magnetic field dependence of $\tau(H)$ with field direction at $\sim 0° \leqslant \theta \leqslant 30°$ and $40° \leqslant \theta \leqslant 90°$, respectively. Here, θ represents the angle between H and the c axis [see the inset of Fig. 2(a)]. Note that (1) $\tau(H)$ is small and negative with oscillations for $\theta \sim 0°$, (2) $\tau(H)$ increases with increasing H for each θ greater than $0°$, and (3) $\tau(H)$ varies nonmonotonically with θ at each field. To reveal the feature more clearly, we present the angle dependence of $\tau(H, \theta)$ at $H = 5, 15, 25,$ and 35 T in Fig. 2(c). Note that the maximum torque occurs around $40°$ in low magnetic field and tends to saturate at 35 T below $40°$. This implies that
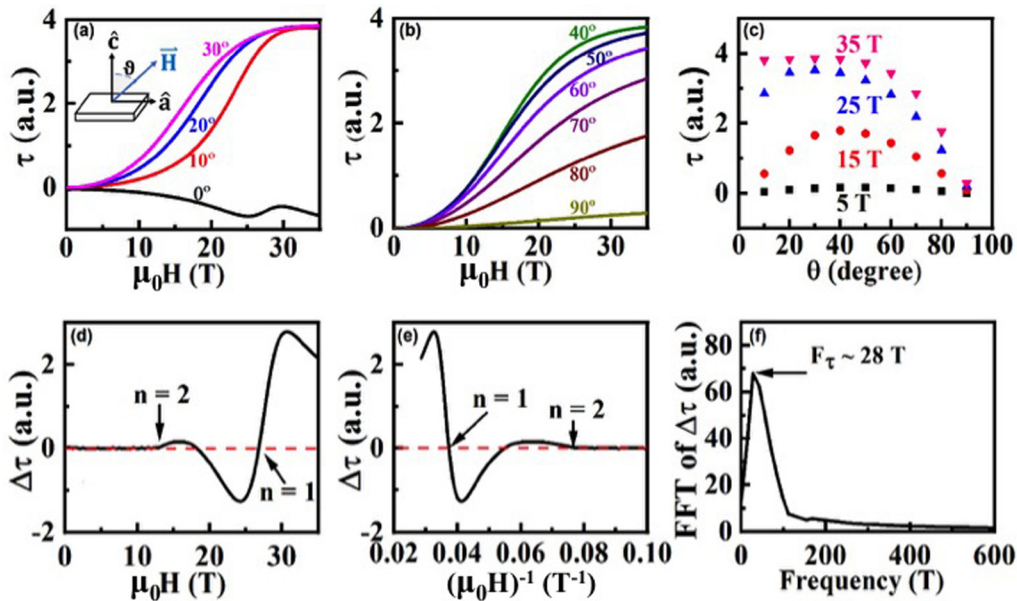
FIG. 2. [(a) and (b)] Magnetic field dependence of the torque τ at 2 K at $\sim 0° \leqslant \theta \leqslant 30°$ (a) and $40° \leqslant \theta \leqslant 90°$ (b). (c) Angular dependence of τ at 2 K under $H = 5$, 15, 25, and 35 T. (d) Field dependence of $\Delta\tau$ at $\sim 0°$. (e) $\Delta\tau$ vs H^{-1} at $\sim 0°$. (f) FFT of the oscillatory $\Delta\tau$ at $\sim 0°$.

the canted spin angle is $\sim 50°$ from the c axis, given that $\vec{\tau} = \vec{M} \times \vec{H}$.

We now focus on the $\theta \sim 0°$ case with the negative torque. This implies that the actual $\theta < 0°$, equivalent to the application of a negative magnetic field. What is remarkable is the oscillation of $\tau(H)$ under high magnetic field, which vanishes when magnetic field direction is slightly away from the c axis. This is due to the decrease of the oscillation amplitude and the increase of contribution from the magnetic moments. The oscillatory component of the torque obtained by subtracting the background is shown in Figs. 2(d) and 2(e), where the integer n represents the Landau level (LL). The LL assignment is based on our previous study with $n = 2$ at $H \sim 12.5$ T [14]. The application of high magnetic field allows to reach the first LL as indicated. The fast Fourier transformation (FFT) yields a single frequency $F_\tau \sim 28$ T, which is slightly higher than the frequency obtained from Shubnikov-de Haas (SdH) oscillations (see below). According to the Onsager relation $F \propto A_F$, higher F_τ would correspond to a larger Fermi surface cross-sectional area (A_F) normal to the magnetic field. Slight nonstoichiometry in the sample for the torque measurement could have shifted the Fermi level down, resulting in larger A_F. On the other hand, the FFT covers less than two periodicities, which can result in large error in F_τ due to error introduced in the background subtraction. As shown in Fig. 2(a), $\tau(H, \theta > 0°)$ exhibits metamagnetic-like field dependence. It is impossible to incorporate such feature in our background subtraction in $\tau(H, \theta \sim 0°)$, thus affecting F_τ.

While the system is pushed down to the first LL, there is no sign for any additional feature in $\Delta\tau$ [see Figs. 2(d) and 2(e)]. We further carried out magnetotransport measurements up to 35 T. Figure 3(a) shows the magnetic field dependence of $\rho_{ab}(H)$ between 1.3 and 50 K with $H \parallel c$. Similar to our previous observation below 14 T [14], $\rho_{ab}(H)$ exhibits the

SdH oscillations, which become even more profound under higher field. To help understand the high-field effect, we isolate the oscillatory component ($\Delta\rho_{ab}$) by subtracting the background, which is plotted as a function of H^{-1} in Fig. 3(b). While it oscillates with H^{-1} as expected down to the second LL ($n = 2$), the peak corresponding to $n = 1$ splits into two shoulders (indicated by up and down arrows), which become more profound with decreasing temperature. To figure out the high-field behavior, we fit $\Delta\rho_{ab}$ using the Lifshitz-Kosevich
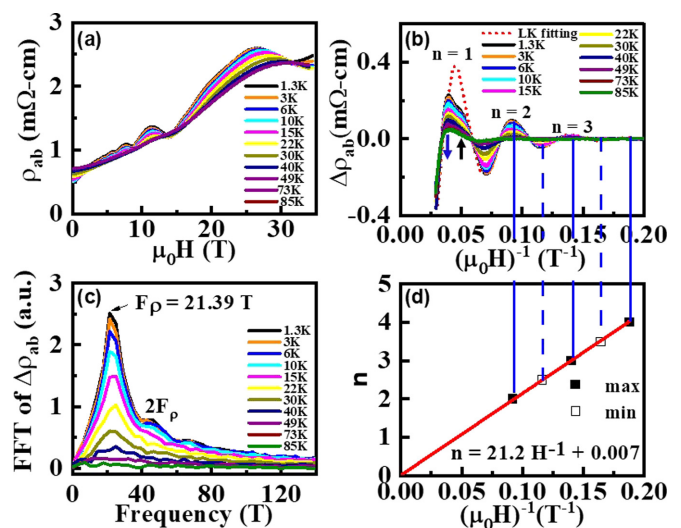

FIG. 3. (a) $\rho_{ab}(H)$ at indicated temperatures. (b) $\Delta\rho_{ab}$ as a function of H^{-1} at indicated temperatures. The red dashed line represents the LK formula at 1.3 K. Arrows indicate spin-up and spin-down shoulders. (c) FFT of $\Delta\rho_{ab}$ at indicated temperatures. (d) Landau level fan diagram obtained from $\Delta\rho_{ab}$.
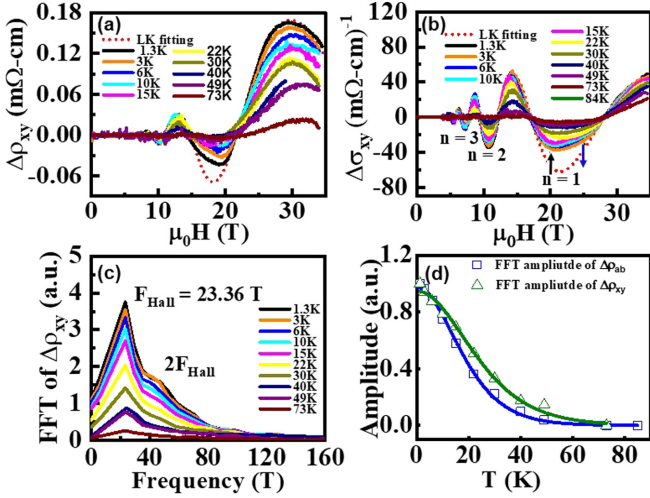
FIG. 4. (a) Magnetic field dependence of the oscillatory Hall resistivity $\Delta\rho_{xy}$ at indicated temperatures. The dashed line represents the LK formula at 1.3 K. (b) Magnetic field dependence of the oscillatory Hall conductivity $\Delta\sigma_{xy}$ at indicated temperatures. The dashed line represents the LK formula at 1.3 K. Arrows indicate spin-up and spin-down valleys. (c) FFT of oscillatory $\Delta\rho_{xy}$ at indicated temperatures. (d) Temperature dependence of the oscillation amplitude of $\Delta\rho_{ab}$ (black squares) and $\Delta\rho_{xy}$ (red triangles) normalized with respect to the amplitude at 1.3 K. (Inset) Normalized FFT amplitude as a function of T for $\Delta\rho_{ab}$ (black squares) and $\Delta\rho_{xy}$ (red triangles).

(LK) formula [20]

$$\Delta\rho \propto \frac{\lambda T}{\sinh(\lambda T)} e^{-\lambda T_{\mathrm{D}}} \cos\left[2\pi\left(\frac{F}{H} - \frac{1}{2} + \delta\right)\right]. \quad (1)$$

Here, $\lambda = (2\pi^2 k_B m^*)/(\hbar e H)$, m^* is the effective mass of electrons, δ is the phase factor, and T_D is the Dingle temperature. The dashed line in Fig. 3(b) represents the LK fitting to the oscillation without considering the LL splitting. Note that the two shoulders are located on each side of the LK peak for $n = 1$. This suggests that the peak splitting is caused by Zeeman energy ($\Delta\varepsilon \sim g\mu_B H$, with g being the Landé factor), which is strong enough under high magnetic field to overcome the thermal broadening of the first LL at low temperatures. Such splitting would result in a peak in the fast Fourier transformation (FFT), corresponding to $2F_\rho$. As shown in Fig. 3(c), the $2F_\rho$ peaks emerge below 15 K. From $\Delta\rho_{ab}$, we obtain a single frequency $F_\rho \sim 21.4$ T. To confirm the value of F_ρ, we further construct the Landau fan diagram in Fig. 3(d) using data above the first LL. Fitting data with the Lifshitz-Onsager relation $n = F/H - \frac{1}{2} + \delta$, we obtain $-\frac{1}{2} + \delta = 0.007$ and $F_\rho \sim 21.2$ T. The frequency agrees very well with that from FFT.

At the first LL, the shoulders caused by Zeeman splitting occur at $H_+ \sim 20$ T (spin up) and $H_- \sim 25$ T (spin down). To confirm this feature, we further analyze the Hall resistivity $\rho_{xy}(H)$. Figure 4(a) shows the magnetic field dependence of the oscillatory $\Delta\rho_{xy}(H)$ (after subtracting the background) at temperatures between 1.3 and 75 K. Deviation from normal oscillation is noticeable above 14 T. Since $\rho_{xy} \ll \rho_{ab}$, the Hall

resistivity is converted to the Hall conductivity via $\sigma_{xy}(H) = \rho_{xy}/(\rho_{ab}^2 + \rho_{xy}^2)$. Figure 4(b) displays the oscillatory $\Delta\sigma_{xy}$ (after subtracting the background) plotted as a function of H. Similar to what is seen in $\Delta\rho_{ab}$, $\Delta\sigma_{xy}$ clearly shows splitting at $n = 1$ (at the valley) located at $H_+ \sim 20$ T (spin up) and $H_- \sim 25$ T (spin down). Applying FFT analyses to $\Delta\rho_{xy}$, there is only one peak corresponding to frequency $F_{\mathrm{Hall}} \sim 23.4$ T, slightly higher than that obtained from $\Delta\rho_{ab}$. The weaker peak corresponds to $2F_{\mathrm{Hall}}$ due to Zeeman splitting. It should be pointed out that smooth background curves were used for obtaining $\Delta\rho_{ab}$ and $\Delta\rho_{xy}$. The *actual* background may not be as smooth as we used, because of possible response to the metamagnetic-like transition between 10–25 T [see Fig. 2(a)]. If this is indeed the case, it will introduce error in the oscillatory amplitude in this field region, but not the periodicity and Zeeman splitting peaks.

The observation of Zeeman splitting implies that the Zeeman energy is greater than the Landau level breadth. The g factor can be estimated via $\frac{gm^*}{2m_0} = \frac{F}{H_+} - \frac{F}{H_-}$ [21]. The effective mass can be estimated by analyzing the temperature dependence of the FFT amplitude using Eq. (1). The solid curves in Fig. 4(d) are the fitting results, with fitting parameter $m^* \sim 0.042 m_0$ (from FFT of $\Delta\rho_{ab}$) and $0.049 m_0$ (from FFT of $\Delta\rho_{xy}$). Thus we obtain $g \sim 8.9$ from $m^* \sim 0.049 m_0$ and ~ 10.4 for $m^* \sim 0.042 m_0$. While it is greater than the free electron case with $g = 2$, the g factor for BaMnSb$_2$ is small compared to Dirac semimetals such as ZrTe$_5$ ($g \sim 15$) [22], ZrSiS ($g \sim 38$) [23], and Cd$_3$As$_2$ ($g \sim 22$) [24]. The moderate g factor suggests moderate electron-electron interaction in the first LL of BaMnSb$_2$.

IV. CONCLUSION

We have investigated the thermal, magnetic, and magneto-transport properties of BaMnSb$_2$ in a wide temperature and magnetic field range. Several new features are observed. First, BaMnSb$_2$ exhibits the very low phonon thermal conductivity at room temperature, likely due to its layered structure. Second, BaMnSb$_2$ has complex magnetic structures with three magnetic phases: in addition to known canted antiferromagnetic state below $T_{N1} \sim 286$ K, there are two other transitions with an antiferromagnetic ordering at $T_{N2} \sim 450$ K and a ferromagnetic ordering at $T_C \sim 690$ K. At 2 K, the angle dependence of the magnetic torque in fields between 0 and 35 T reveals that the spin canting angle is about 50° from the c axis. Furthermore, the field dependence of the magnetic torque $\tau(H)$ and magnetoresistance reveals the dHvA and SdH oscillations with $H \parallel c$. The dHvA oscillation can no longer be seen when H is slightly away from the c axis, likely due to the large background. Magnetic field up to 35 T pushes electrons beyond the first LL, where Zeeman splitting is observed. The analyses of Zeeman splitting reveal the Landé g factor 8.9–10.4.

[1] P. A. M. Dirac, Proc. R. Soc. Lond. A **117**, 610 (1928).

[2] H. Weyl, Proc. Natl. Acad. Sci. USA **15**, 323 (1929).

[3] S. M. Young, S. Zaheer, J. C. Y. Teo, C. L. Kane, E. J. Mele, and A. M. Rappe, Phys. Rev. Lett. **108**, 140405 (2012).

[4] A. Wang, D. Graf, L. Wu, K. Wang, E. Bozin, Y. Zhu, and C. Petrovic, Phys. Rev. B **94**, 125118 (2016).

[5] J. B. He, Y. Fu, L. X. Zhao, H. Liang, D. Chen, Y. M. Leng, X. M. Wang, J. Li, S. Zhang, M. Q. Xue *et al.*, Phys. Rev. B **95**, 045128 (2017).

[6] K. Wang, D. Graf, H. Lei, S. W. Tozer, and C. Petrovic, Phys. Rev. B **84**, 220401(R) (2011).

[7] J. Park, G. Lee, F. Wolff-Fabris, Y. Y. Koh, M. J. Eom, Y. K. Kim, M. A. Farhan, Y. J. Jo, C. Kim, J. H. Shim, and J. S. Kim, Phys. Rev. Lett. **107**, 126402 (2011).

[8] A. F. May, M. A. McGuire, and B. C. Sales, Phys. Rev. B **90**, 075109 (2014).

[9] S. Borisenko, D. Evtushinsky, Q. Gibson, A. Yaresko, K. Koepernik, T. Kim, M. Ali, J. V. D. Brink, M. Hoesch, A. Fedorov *et al.*, Nat. Commun. **10**, 3424 (2019).

[10] Y. Liu, T. Ma, L. Zhou, W. E. Straszheim, F. Islam, B. A. Jensen, W. Tian, T. Heitmann, R. A. Rosenberg, J. M. Wilde *et al.*, Phys. Rev. B **99**, 054435 (2019).

[11] C. Yi, S. Yang, M. Yang, L. Wang, Y. Matsushita, S. Miao, Y. Jiao, J. Cheng, Y. Li, K. Yamaura *et al.*, Phys. Rev. B **96**, 205103 (2017).

[12] Y.-Y. Wang, S. Xu, L.-L. Sun, and T.-L. Xia, Phys. Rev. Mater. **2**, 021201(R) (2018).

[13] J. Y. Liu, J. Hu, Q. Zhang, D. Graf, H. B. Cao, S. M. A. Radmanesh, D. J. Adams, Y. L. Zhu, G. F. Cheng, X. Liu *et al.*, Nat. Mater. **16**, 905 (2017).

[14] S. Huang, J. Kim, W. A. Shelton, E. W. Plummer, and R. Jin, Proc. Natl. Acad. Sci. USA **114**, 6256 (2017).

[15] H. Masuda, H. Sakai, M. Tokunaga, Y. Yamasaki, A. Miyake, J. Shiogai, S. Nakamura, S. Awaji, A. Tsukazaki, H. Nakao, Y. Murakami, T. Arima, Y. Tokura, and S. Ishiwata, Sci. Adv. **2**, e1501117 (2016).

[16] J. Liu, J. Hu, H. Cao, Y. Zhu, A. Chuang, D. Graf, D. J. Adams, S. M. A. Radmanesh, L. Spinu, I. Chiorescu *et al.*, Sci. Rep. **6**, 30525 (2016).

[17] Z. Wang, R. Jin, L. Wu, J. Tao, A. B. Karki, J. Y. Pan, Y. Zhu, and E. W. Plummer, Phys. Rev. B **100**, 094103 (2019).

[18] I. Teramoto and A. V. Run, Phys. Chem. Solids **29**, 347 (1968).

[19] J. B. He, D. M. Wang, and G. F. Chen, Appl. Phys. Lett. **100**, 112405 (2012).

[20] I. M. Lifshitz and A. M. Kosevich, J. Phys. Chem. Solids **4**, 1 (1958).

[21] G. W. Semenoff, Phys. Rev. Lett. **53**, 2449 (1984).

[22] J. L. Zhang, C. Y. Guo, X. D. Zhu, L. Ma, G. L. Zheng, Y. Q. Wang, L. Pi, Y. Chen, H. Q. Yuan, and M. L. Tian, Phys. Rev. Lett. **118**, 206601 (2017).

[23] J. Hu, Z. Tang, J. Liu, Y. Zhu, J. Wei, and Z. Mao, Phys. Rev. B **96**, 045127 (2017).

[24] Z. J. Xiang, D. Zhao, Z. Jin, C. Shang, L. K. Ma, G. J. Ye, B. Lei, T. Wu, Z. C. Xia, and X. H. Chen, Phys. Rev. Lett. **115**, 226401 (2015).